

# Cartesian Grid Method for Compressible Flow Using Simplified Ghost Point Treatments at Embedded Boundaries

Are Arstad Skøien and Bernhard Müller

Department of Energy and Process Engineering, Faculty of Engineering Science and Technology,  
The Norwegian University of Science and Technology, NO-7491 Trondheim, Norway  
e-mail: are.skøien@gmail.com, e-mail: bernhard.muller@ntnu.no

**Summary** A Cartesian grid method has been developed for solving the 2D Euler and Navier-Stokes equations for inviscid and viscous compressible flow, respectively. Using simplified ghost point treatments, we choose the closest grid points as mirror points of the ghost points. Wall boundary conditions are implemented by imposing symmetry conditions at the ghost points of the embedded boundary. The accuracy of the method has been investigated for various test cases. We show computed examples of supersonic inviscid flow past a diamond-wedge airfoil and a circular cylinder. The method is also tested for supersonic laminar flow over a cylinder, for which the computed skin friction profiles have been used to assess the accuracy. Supersonic laminar flow around a NACA0012 airfoil is computed, and the lift and drag coefficients along with the pressure coefficient profile are compared with the literature. Lastly, supersonic flow around a 2D model of the F-22 fighter aircraft with simulated jet engine outflow is chosen to illustrate the flexibility of the method. For inviscid flow, the results obtained with our simplified ghost point treatments are comparable to results with other more complex Cartesian grid methods. For viscous flow, however, a more accurate treatment of the boundary conditions at body surfaces is needed.

## Introduction

The Cartesian grid method has recently become a popular method in CFD to compute flows over or in complex geometries [11, 5, 4, 9, 15, 10, 2, 14]. The reason lies in its simplification of grid generation, lower storage requirements, lower operation count, and easier post processing compared to body-fitted structured and unstructured grid methods. The Cartesian grid method is also advantageous in constructing higher order methods. Adding an additional body with the body-fitted method means redoing the entire grid, but with the Cartesian grid method investigated here this can be done in a few simple steps. Instead of generating a body-fitted structured or unstructured grid, the body is embedded in a simple Cartesian grid and the effect of the body is taken into account by proper conditions at grid points near the body surface. When the Cartesian grid method is applied at curved boundaries the cells at the boundaries are not rectangular and these cut-cells create problems for the scheme to be implemented. These problems are not present in the simplified ghost point treatment, as symmetry conditions with respect to the boundary are imposed at ghost points inside the body adjacent to the boundary.

The simplified ghost point method has been verified for the 2D compressible Euler equations considering transonic flow over a circular arc bump in a channel and supersonic flow over a circular arc airfoil and a circular cylinder [7, 8, 6]. For the inviscid Burgers' equation and the 1D compressible Euler equations, the convergence rate of the present Cartesian grid method has been shown to be similar to corresponding body-fitted grid methods [6]. A new simplified ghost point method has been developed in [16] and is presented here. Extensive numerical tests have been performed to demonstrate the properties of the method. We consider steady supersonic inviscid flow over a diamond-wedge airfoil and a circular cylinder. Moreover, steady supersonic laminar flow over a circular cylinder and a NACA0012 airfoil are simulated using the new simplified ghost point method. The last example is steady supersonic inviscid flow around a 2D model of the F-22 fighter aircraft with two jet engines firing. The method experiences some problems for the skin friction profile on the circular cylinder, seen as unwanted bumps in the

profile, but the computed results are overall in good agreement with those obtained from other work and available analytical data.

The outline of the paper is as follows. In section 'Governing Equations', the compressible Euler and Navier-Stokes equations are given. The discretization in space and time is presented in section 'Numerical Discretization'. The ghost point treatment at embedded boundaries of the present Cartesian grid method is outlined in section 'Ghost Point Treatment'. The verification of the present ghost point treatment is presented and discussed in section 'Results'. Conclusions are given in the last section.

## Governing Equations

The 2D compressible Navier-Stokes equations in conservative form can be expressed as

$$\mathbf{U}_t + \mathbf{F}_x + \mathbf{G}_y = 0, \quad (1)$$

where  $\mathbf{U}$  is the vector of the conservative variables.  $\mathbf{F} = \mathbf{F}^c - \mathbf{F}^v$  and  $\mathbf{G} = \mathbf{G}^c - \mathbf{G}^v$  denote the differences of the inviscid and viscous flux vectors in the  $x$ - and  $y$ -directions, respectively. The subscripts of the flux vectors in (1) and subsequently denote derivatives. The conservative variables and the flux vectors are defined by

$$\mathbf{U} = \begin{pmatrix} \rho \\ \rho u \\ \rho v \\ \rho E \end{pmatrix}, \quad \mathbf{F}^c = \begin{pmatrix} \rho u \\ \rho u u + p \\ \rho v u \\ \rho H u \end{pmatrix}, \quad \mathbf{G}^c = \begin{pmatrix} \rho v \\ \rho u v \\ \rho v v + p \\ \rho H v \end{pmatrix}$$

$$\mathbf{F}^v = \begin{pmatrix} 0 \\ \tau_{xx} \\ \tau_{yx} \\ \tau_{xx}u + \tau_{yx}v + \kappa T_x \end{pmatrix}, \quad \mathbf{G}^v = \begin{pmatrix} 0 \\ \tau_{xy} \\ \tau_{yy} \\ \tau_{xy}u + \tau_{yy}v + \kappa T_y \end{pmatrix}.$$

$u$  and  $v$  denote the  $x$ - and  $y$ -components of the velocity.  $\rho$ ,  $p$ ,  $T$  and  $E$  signify the density, pressure, temperature and specific total energy, respectively.  $H = E + \frac{p}{\rho}$  is the total enthalpy. Perfect gas is assumed with the ratio of specific heats  $\gamma = 1.4$  for air. Then, the pressure can be expressed as  $p = (\gamma - 1)(\rho E - \frac{1}{2}\rho(u^2 + v^2))$ . The viscous stress tensor for a Newtonian fluid is given by  $\boldsymbol{\tau} = \mu(\nabla \mathbf{u} + (\nabla \mathbf{u})^T) - \frac{2}{3}\mu \nabla \cdot \mathbf{u} \mathbf{I}$ , where  $\mathbf{I}$  denotes the unit tensor. Thereby, the components of  $\boldsymbol{\tau}$  in Cartesian coordinates  $\tau_{ij}$  above are defined. The viscosity coefficient  $\mu$  is determined from the Sutherland law and the heat conduction coefficient  $\kappa$  by assuming the Prandtl number to be constant, namely  $\text{Pr} = 0.72$ .

The 2D compressible Euler equations in conservative form can be expressed as

$$\mathbf{U}_t + \mathbf{F}_x^c + \mathbf{G}_y^c = 0. \quad (2)$$

## Numerical Discretization

### Spatial Discretization

The node-centered finite volume method has been used for the spatial discretization. At a Cartesian grid point  $(x_i, y_j)$ , where  $x_i = x_a + (i - 1)\Delta x$  and  $y_j = y_a + (j - 1)\Delta y$ ,  $i = 1, \dots, N$ ,  $j = 1, \dots, M$ , the semi-discretization of the 2D compressible Navier-Stokes equations (1) reads

$$\frac{d\mathbf{U}_{i,j}}{dt} = -\frac{\mathbf{F}_{i+\frac{1}{2},j} - \mathbf{F}_{i-\frac{1}{2},j}}{\Delta x} - \frac{\mathbf{G}_{i,j+\frac{1}{2}} - \mathbf{G}_{i,j-\frac{1}{2}}}{\Delta y}, \quad (3)$$

where  $\mathbf{U}_{i,j}$  is the approximation of the average of  $\mathbf{U}$  in the cell

$\Omega_{i,j} = [x_i - \frac{\Delta x}{2}, x_i + \frac{\Delta x}{2}] \times [y_j - \frac{\Delta y}{2}, y_j + \frac{\Delta y}{2}]$ , i.e.

$$\mathbf{U}_{i,j} \approx \frac{1}{\Delta x \cdot \Delta y} \int_{\Omega_{i,j}} \mathbf{U}(x, y, t) \, dx dy. \quad (4)$$

The numerical fluxes of the local Lax-Friedrichs method for the inviscid flux vectors  $\mathbf{F}^c$  and  $\mathbf{G}^c$  are defined as follows

$$\mathbf{F}_{i+\frac{1}{2},j}^c = \frac{1}{2} [\mathbf{F}^c(\mathbf{U}_{i,j}) + \mathbf{F}^c(\mathbf{U}_{i+1,j}) - \max(|u_{i+1,j}| + c_{i+1,j}, |u_{i,j}| + c_{i,j})(\mathbf{U}_{i+1,j} - \mathbf{U}_{i,j})], \quad (5)$$

$$\mathbf{G}_{i,j+\frac{1}{2}}^c = \frac{1}{2} [\mathbf{G}^c(\mathbf{U}_{i,j}) + \mathbf{G}^c(\mathbf{U}_{i,j+1}) - \max(|v_{i,j+1}| + c_{i,j+1}, |v_{i,j}| + c_{i,j})(\mathbf{U}_{i,j+1} - \mathbf{U}_{i,j})]. \quad (6)$$

In equations (5) and (6),  $c$  is the speed of sound.

The first order approximation of the inviscid flux (5) at cell face  $x_{i+\frac{1}{2},j}$  can be easily extended to second order, except for extrema, by van Leer's MUSCL (Monotone Upstream-centered Schemes for Conservation Laws) approach. The states  $\mathbf{U}_{i,j}$  and  $\mathbf{U}_{i+1,j}$  in (5) are replaced by the extrapolated values  $\mathbf{U}_{i+\frac{1}{2},j}^L$  and  $\mathbf{U}_{i+\frac{1}{2},j}^R$ , respectively. The latter are defined by:

$$\mathbf{U}_{i+\frac{1}{2},j}^L = \mathbf{U}_{i,j} + \frac{1}{2} \min\text{mod}(\mathbf{U}_{i,j} - \mathbf{U}_{i-1,j}, \mathbf{U}_{i+1,j} - \mathbf{U}_{i,j}), \quad (7)$$

$$\mathbf{U}_{i+\frac{1}{2},j}^R = \mathbf{U}_{i+1,j} - \frac{1}{2} \min\text{mod}(\mathbf{U}_{i+2,j} - \mathbf{U}_{i+1,j}, \mathbf{U}_{i+1,j} - \mathbf{U}_{i,j}), \quad (8)$$

where

$$\begin{aligned} \min\text{mod}(a, b) &= \begin{cases} a & \text{if } |a| \leq |b| \text{ and } ab > 0 \\ b & \text{if } |b| < |a| \text{ and } ab > 0 \\ 0 & \text{if } ab \leq 0 \end{cases} \quad (9) \\ &= \text{sign}(a) \max\{0, \min\{|a|, \text{sign}(a)b\}\} \end{aligned}$$

is the minmod limiter. The MUSCL approach is applied similarly to the numerical fluxes  $\mathbf{G}_{i,j+\frac{1}{2}}^c$  in (6).

The viscous fluxes  $\mathbf{F}_{i+\frac{1}{2},j}^v$  and  $\mathbf{G}_{i,j+\frac{1}{2}}^v$  are approximated by standard second order central finite differences [16].

### Time Discretization

The spatial discretization above leads to a system of ordinary differential equations (ODEs)

$$\frac{d\mathbf{U}}{dt} = \mathbf{R}(\mathbf{U}), \quad (10)$$

where  $\mathbf{U} = (\mathbf{U}_{i,j})$  is the grid function of the conservative variables and  $\mathbf{R} = (\mathbf{R}_{i,j})$  the grid function of the residuals with the residual  $\mathbf{R}_{i,j}$  defined by the right hand side of equation (3).

The system of ODEs (10) is solved by the third order total variation diminishing Runge-Kutta method (TVD RK3)

$$\begin{aligned}\mathbf{U}^{(1)} &= \mathbf{U}^n + \Delta t \mathbf{R}(\mathbf{U}^n), \\ \mathbf{U}^{(2)} &= \frac{3}{4} \mathbf{U}^n + \frac{1}{4} \mathbf{U}^{(1)} + \frac{1}{4} \Delta t \mathbf{R}(\mathbf{U}^{(1)}), \\ \mathbf{U}^{(n+1)} &= \frac{1}{3} \mathbf{U}^n + \frac{2}{3} \mathbf{U}^{(2)} + \frac{2}{3} \Delta t \mathbf{R}(\mathbf{U}^{(2)}).\end{aligned}\quad (11)$$

The stability of the time stepping method is dependent on the eigenvalues of the Jacobian matrices of the flux vectors and the properties of the space and time discretization methods. To make sure not to take a too large time step the Courant-Friedrichs-Lewy (CFL) number and the von Neumann number (VNN) are used. For the 2D compressible Navier-Stokes they are defined as follows [12]

$$\text{CFL} = \Delta t_c \max_{i,j} \left( \frac{|u| + c}{\Delta x} + \frac{|v| + c}{\Delta y} \right)_{i,j}, \quad (12)$$

$$\text{VNN} = \Delta t_v \left( \frac{1}{\Delta x^2} + \frac{1}{\Delta y^2} \right) \max \left( \frac{4}{3}, \frac{\gamma}{\text{Pr}} \right) \max_{i,j} \left( \frac{\mu}{\rho} \right)_{i,j}. \quad (13)$$

The CFL and VNN numbers are then set for each simulation. The VNN has been set as 0.4, while the CFL number is varied from 0.5 to 0.25, depending on the simulation. The time step sizes  $\Delta t_c$  and  $\Delta t_v$  are calculated from the CFL and VNN numbers for every time step and the minimum of both is chosen as  $\Delta t$  in the TVD RK3.

## Ghost Point Treatment

### Simplified Ghost Point Treatment for Embedded Boundary in 2D

In the simplified ghost point treatment, the fluid point F adjacent to the embedded boundary is chosen as a mirror point [7, 8, 6]. The embedded boundary is assumed to lie in the middle between ghost and fluid points. In figure 1 the idea is shown on a  $9 \times 9$  grid.

For inviscid flow, the primitive variables at the ghost points are set as

$$\rho_G = \rho_F, p_G = p_F, u_G = u_F - 2(n_1 u_F + n_2 v_F)n_1, v_G = v_F - 2(n_1 u_F + n_2 v_F)n_2, \quad (14)$$

assuming the embedded boundary to be a symmetry boundary lying in the middle between ghost point G and mirror point F. Then, the arithmetic average of the normal velocities at G and F is zero. That is the correct boundary condition for an impermeable boundary.

For viscous flow, the primitive variables at the ghost points are set as

$$\rho_G = \rho_F, p_G = p_F, u_G = -u_F, v_G = -v_F, \quad (15)$$

assuming the embedded boundary to lie in the middle between ghost point G and mirror point F. At the embedded boundary, the no-slip condition  $u = v = 0$  and the conditions  $\partial\rho/\partial n = \partial p/\partial n = 0$  are assumed. The wall boundary condition  $\partial p/\partial n = 0$  is an approximation of the normal momentum equation for high Reynolds numbers. If the wall is adiabatic, i.e.  $\partial T/\partial n = 0$ , the homogeneous Neumann boundary condition for the density follows from  $\partial p/\partial n = 0$  and the equation of state for perfect gas  $p = \rho RT$ , where  $R$  is the gas constant for air.

The mirror points F have to be chosen carefully. On the west side of the domain the ghost point values are calculated using the values at the fluid points to the west of the ghost points:

$$U_{iG,jG} = U_{iG-1,jG}.$$

On the south side of the domain the ghost points are calculated using the fluid points south of the ghost points:  $U_{iG,jG} = U_{iG,jG-1}$ . On the east side of the domain the ghost points are calculated using the fluid points to the east of the ghost points:  $U_{iG,jG} = U_{iG+1,jG}$ . On the north side of the domain the ghost points are calculated using the fluid points to the north of the ghost points:

$$U_{iG,jG} = U_{iG,jG+1}.$$

Four points on the grid are located exactly on the circle, i.e. the intersection of the grid lines through the center point  $(a, b)$  with the circle. These have to be taken care of explicitly and are set as fluid points, cf. figure 1.

Four ghost points on the grid are located on the 45-degree intersection lines. On this line a ghost point can be calculated using the nearest fluid points either in the x-direction or in the y-direction. In the present approach these ghost points are calculated using the nearest fluid points lying in the x-direction. Another approach could be to choose the nearest fluid points lying on the intersection line, i.e. the diagonal.

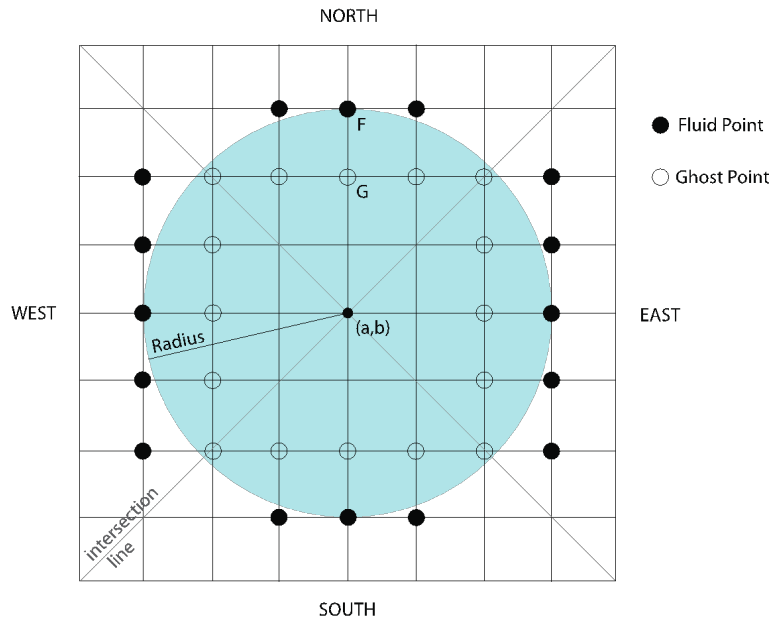


Figure 1: Illustration of the fluid points chosen as mirror points and the ghost points set to embed a solid cylinder boundary.

### New Simplified Ghost Point Treatment for Embedded Boundary in 2D

The New Simplified method is developed to be more accurate than the Simplified method. The new method is still very similar, but it will choose its mirror fluid points from more locations

than the old method. Instead of only choosing the mirror points on the grid lines through the ghost points in the x- or y-directions, the new method also considers all diagonal directions. The New Simplified method chooses its mirror fluid points from a total of eight different locations, depending on the unit normal component of the surface nearest to the ghost point. In figure 2 there are two blunt bodies of random shape. Their normal component is calculated on the surface, and the angle of the unit normal is calculated with respect to the negative x-axis such that if  $n_x = -1$  and  $n_y = 0$  then  $\varphi = 0$ .

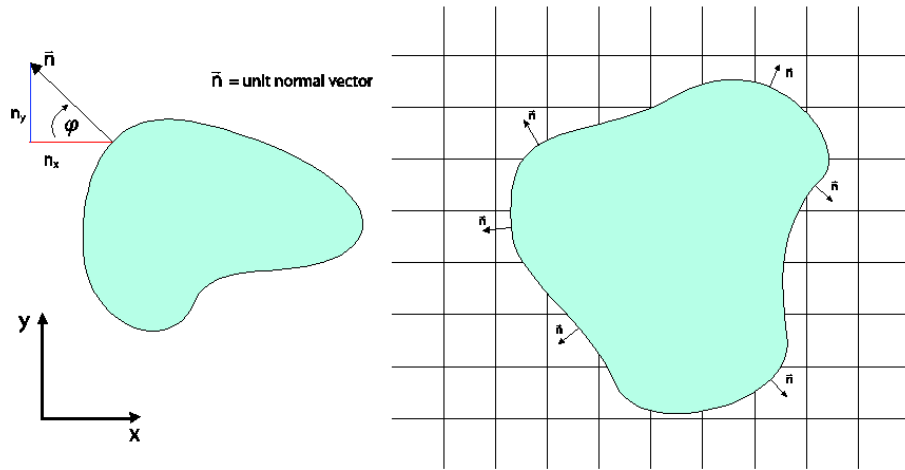


Figure 2: Angle used to identify fluid point (left). Normal components on body (right).

If  $(i, j)$  represents the index of a ghost point then let  $(iF, jF)$  represent the index of the fluid point chosen as the mirror point. The general relationship to choose all fluid point indices is dependent on the angle  $\varphi$  and is given below:

$$\begin{aligned}
 &\text{if } -22.5^\circ < \varphi \leq 22.5^\circ \quad , \text{ then } (iF, jF) = (i - 1, j) \\
 &\text{if } 22.5^\circ < \varphi \leq 67.5^\circ \quad , \text{ then } (iF, jF) = (i - 1, j + 1) \\
 &\text{if } 67.5^\circ < \varphi \leq 112.5^\circ \quad , \text{ then } (iF, jF) = (i, j + 1) \\
 &\text{if } 122.5^\circ < \varphi \leq 157.5^\circ \quad , \text{ then } (iF, jF) = (i + 1, j + 1) \\
 &\text{if } 157.5^\circ < \varphi \leq 202.5^\circ \quad , \text{ then } (iF, jF) = (i + 1, j) \\
 &\text{if } 202.5^\circ < \varphi \leq 247.5^\circ \quad , \text{ then } (iF, jF) = (i + 1, j - 1) \\
 &\text{if } 247.5^\circ < \varphi \leq 292.5^\circ \quad , \text{ then } (iF, jF) = (i, j - 1) \\
 &\text{if } 292.5^\circ < \varphi \leq 337.5^\circ \quad , \text{ then } (iF, jF) = (i - 1, j - 1)
 \end{aligned} \tag{16}$$

For a circular cylinder the fluid points will be chosen as shown in figure 3. In figure 3 the arrows indicate the transfer of fluid data from the mirror points to the ghost points. In this way we can apply the New Simplified method to a variety of different complex geometries.

### Weighted Ghost Point Method

The following method of weighting the ghost point values is only applied to the cylinder due to the added complexity of the method. The wall of the embedded body is identified and the velocities at the ghost points are weighted using a scaling factor in order to improve the accuracy

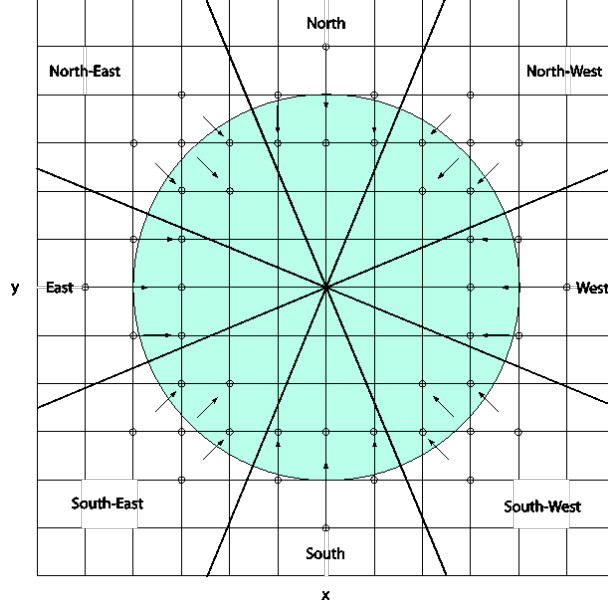


Figure 3: Fluid points (small circles) in white fluid domain used as mirror points for ghost points (small circles) in green solid domain in the New Simplified method.

of the wall boundary treatment. By applying these weights to the velocity components at the ghost points, we try to reflect the embedded boundary closer to its actual location. Without the weights the embedded boundary is assumed to lie in the middle between ghost and fluid points.

The method is illustrated in figure 4. The distance from the ghost point to the embedded wall boundary is called  $a$ , and  $b$  is the distance from the appropriate fluid point to the embedded wall boundary. The distance  $a + b$  is equal to the distance between the ghost point and the corresponding fluid point. The primitive variables at the ghost points for viscous flow are set as

$$\rho_{G1} = \rho_{F1}, p_{G1} = p_{F1}, u_{G1} = -\frac{a}{b}u_{F1}, v_{G1} = -\frac{a}{b}v_{F1}, \quad (17)$$

while with the second order MUSCL scheme the primitive variables for viscous flow are set as

$$\rho_{G2} = \rho_{F2}, p_{G2} = p_{F2}, u_{G2} = -\frac{2a+b}{2b+a}u_{F2}, v_{G2} = -\frac{2a+b}{2b+a}v_{F2}, \quad (18)$$

To avoid instabilities we enforce maximum and minimum values to the scaling  $\frac{a}{b}$  such that

$$\left(\frac{a}{b}\right)_{max} = 2 \quad \text{and} \quad \left(\frac{a}{b}\right)_{min} = 0.5. \quad (19)$$

If the maximum or minimum values are enforced, the distances  $a$  and  $b$  are set to match. For example if  $a = 10$  and  $b = 2$ , then the length  $a$  will be set as  $a = 8$  and the length  $b$  will be set as  $b = 4$ . This must be done to keep the right scaling on the velocities in (18). Note that the normal component at the embedded wall boundary is not used, but only the distance to the wall between the ghost and fluid points. In all test cases featuring a circular cylinder the weighted ghost point method is applied, unless it is stated otherwise.

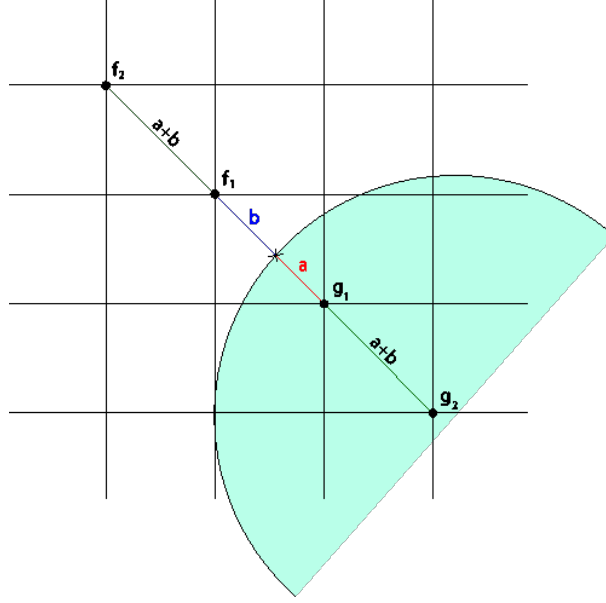


Figure 4: Identifying the weights at the embedded body.

## Results

### *Supersonic Flow around a Diamond-Wedge Airfoil with Compressible Euler Equations*

To test the shock wave behavior of the method a supersonic inviscid flow past a diamond-wedge airfoil has been considered. For this type of flow analytical solutions exist and are compared to the simulations where possible. The simulation has a freestream Mach number  $M_\infty = 3$ , and the deflection angle of the diamond is  $\theta = 15^\circ$ , for which an attached shock at the apex is generated. A grid with  $400 \times 200$  cells has been used to discretize the computational domain  $[-0.75, 3.25] \times [-1, 1]$ . The chord length of the diamond-wedge airfoil is  $c = 2$ , whose leading edge is located at the origin. First order accuracy is used. There are supersonic inflow conditions at  $x = -0.75$ , i.e.  $\mathbf{U}_{1,j} = \mathbf{U}_\infty$ , and supersonic outflow conditions at  $x = 3.25$ , i.e.  $\mathbf{U}_{N,j} = \mathbf{U}_{N-1,j}$ , and at  $y = -1$ , i.e.  $\mathbf{U}_{i,1} = \mathbf{U}_{i,2}$ . The inviscid wall boundary at  $y = 1 - \Delta y/2$  is implemented as a symmetry boundary, i.e. the primitive variables are set like

$$(\rho, u, p)_{i,M} = (\rho, u, p)_{i,M-1}, v_{i,M} = -v_{i,M-1}. \quad (20)$$

For a supersonic flow over a diamond-wedge in a channel, we expect the inviscid flow to develop as illustrated in figure 5. The incident shock will be reflected at the upper wall, and around the top corner of the diamond the supersonic flow will accelerate through expansion waves, as the area in this part increases. Finally an oblique shock wave will settle at the trailing edge where the flow is turned parallel to the x-axis.

The residual of the continuity equation measured as  $\|\rho^{n+1} - \rho^n\|_2$  is reduced by more than six orders of magnitude in 25000 time steps. The convergence history is shown in figure 6. As seen in figure 6, once the flow has settled the solution converges quickly. There are no upstream reflections, because the flow is supersonic at all outflow boundaries.

The calculated incident oblique shock wave angle from the simulation is  $\beta \approx 32^\circ$ , and from the corresponding relation in [1] the shock wave angle should be  $\beta \approx 32.2^\circ$ . Due to the inaccuracy of calculating the shock angle from a simulation result, we are satisfied with this result.

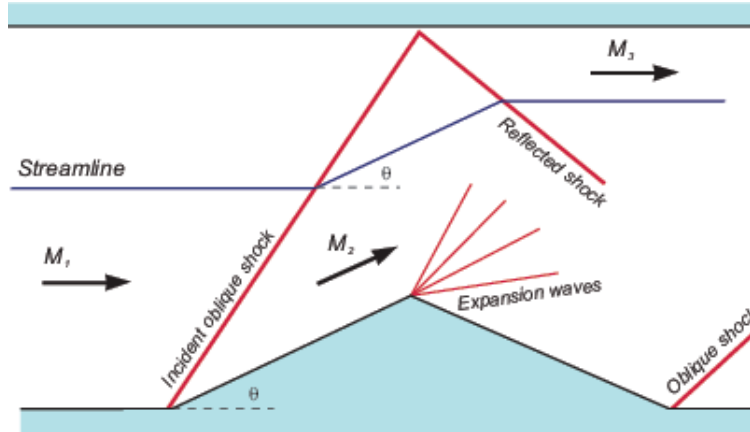


Figure 5: Illustration of expected shock wave behavior in a channel with a diamond-wedge.

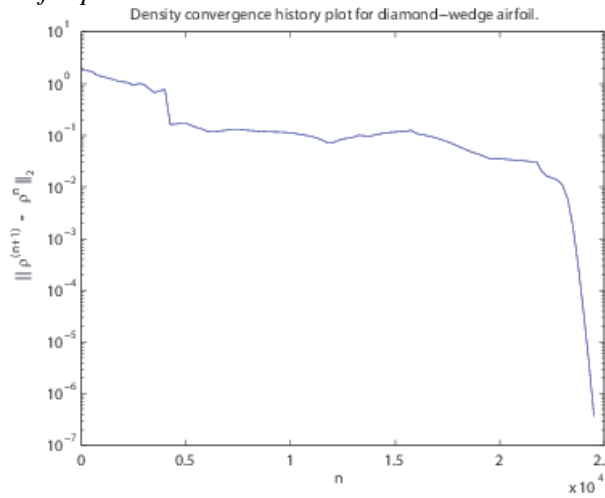


Figure 6: Convergence history for inviscid supersonic flow past a diamond-wedge airfoil at  $M_\infty = 3$  and the deflection angle of the diamond  $\theta = 15^\circ$ .

In figure 7 we observe an attached oblique shock wave at the leading edge of the diamond-wedge airfoil. At the upper wall we see a reflected shock, and at the trailing edge we see oblique shocks attached to the tail of the diamond-wedge. Some shock interactions also occur in the wake, where the reflected shock from the wall intersects the oblique shock from the tail.

### Supersonic Flow over a Circular Cylinder with Compressible Euler Equations

Supersonic inviscid flow past a circular cylinder at  $M_\infty = 3$  has been considered. The computational domain is  $[-2, 2] \times [-2, 2]$ . The diameter of the cylinder is  $D = 1$  and its center is located at  $(x, y) = (0, 0)$ . The boundary conditions for all test cases are for supersonic inflow at the boundary  $x = -2$ , and those for supersonic outflow for all other boundaries. First order accuracy is used.

For this inviscid test case, two grids with  $200 \times 200$  and  $280 \times 280$  cells have been used with the New Simplified method and one case with a grid of  $200 \times 200$  cells has been used with the Simplified method. These simulations have been used to check the pressure coefficient versus Sjögreen and Petersson's results [15] and are shown in figure 8.

The Simplified method has a problem in the area, where the fluid points used to mirror the ghost

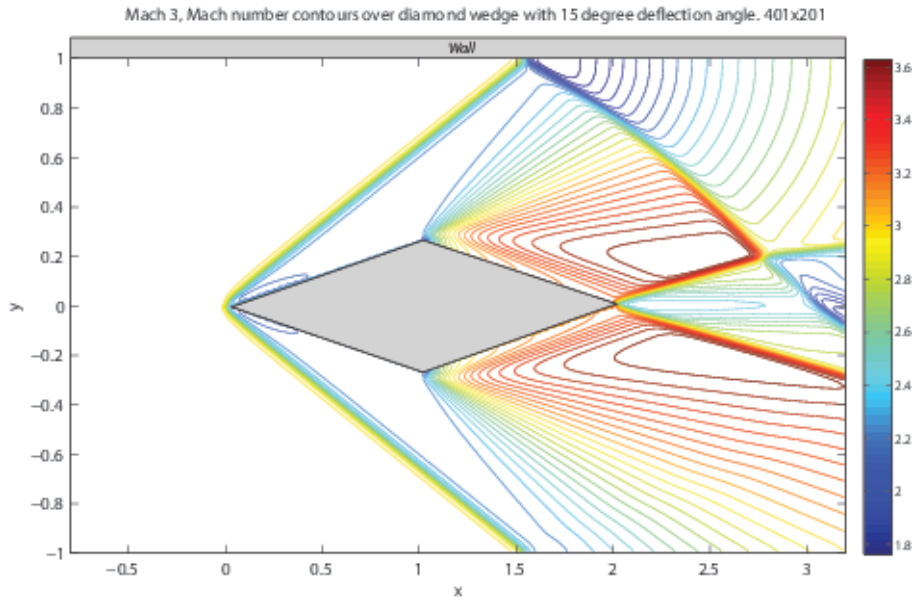


Figure 7: Mach number contours past a diamond-wedge airfoil with attached shock and shock reflection at upper wall boundary for  $M_\infty = 3$  and the deflection angle of the diamond  $\theta = 15^\circ$ .

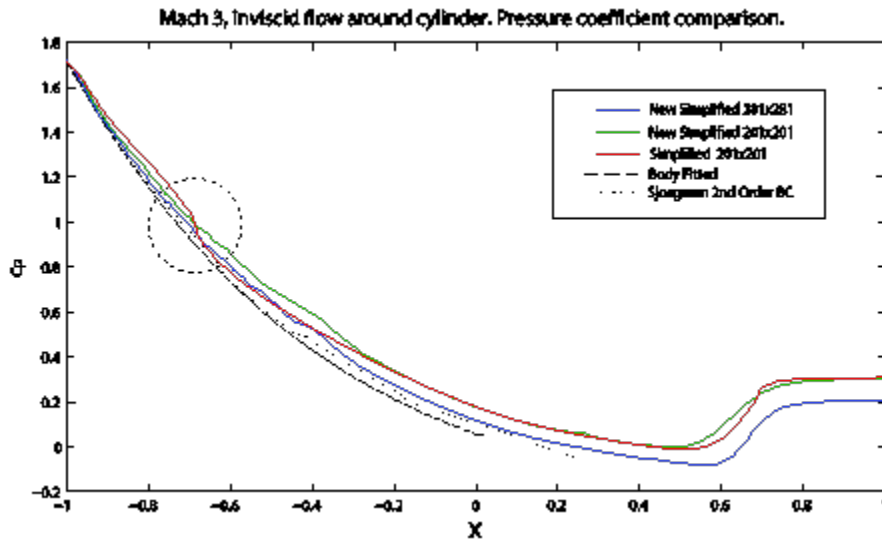


Figure 8: Comparison of the pressure coefficient obtained from the New Simplified method, the Simplified method and the results from Sjogreen and Petersson [15] for inviscid flow over a circular cylinder at  $M_\infty = 3$ .

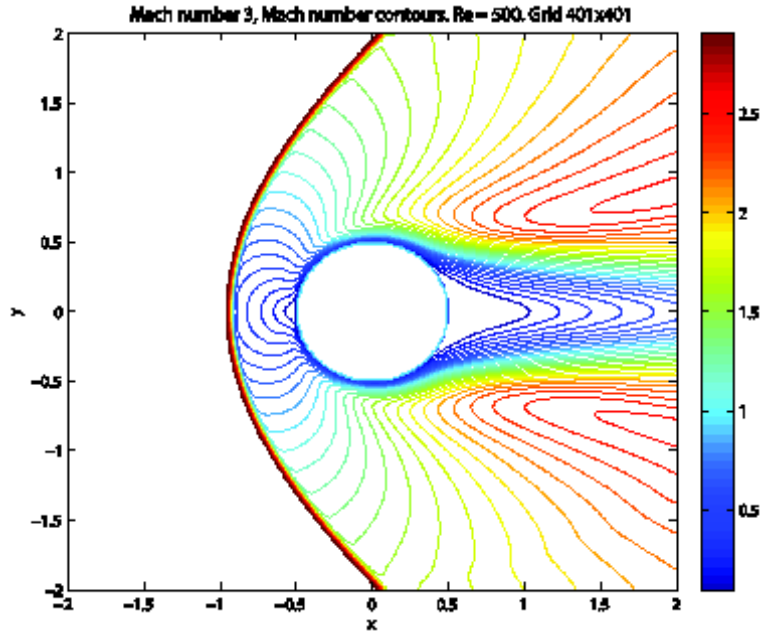


Figure 9: Mach number contours of supersonic flow past an adiabatic circular cylinder at  $M_\infty = 3$  and  $Re_D = 500$  obtained using the New Simplified method.

points change direction from  $x$  to  $y$ . This is seen as a sudden bump in the pressure coefficient near  $x = 0.7$  in figure 8, cf. the region marked by a dashed circle. A goal with developing a new method was to remove that bump. With the New Simplified method that bump is indeed no longer present. The pressure coefficient is slightly higher than the results by Sjögreen and Petersson [15], but with grid refinement the pressure coefficient comes closer to their results. It is worthwhile mentioning that Sjögreen and Petersson [15] used a  $305 \times 200$  grid.

### *Supersonic Flow over a Circular Cylinder with Compressible Navier-Stokes Equations*

The goals in this subsection are:

- 1) To compare the New Simplified method versus the Simplified method,
- 2) To compare the New Simplified method with weighted ghost points versus the New Simplified method without weighted ghost points and
- 3) Test the New Simplified method versus a well documented Cartesian grid method for viscous flow at supersonic flow conditions.

Supersonic flow past a circular cylinder at  $M_\infty = 3$  and  $Re_D = 500$  has been considered. Three grids with  $160 \times 160$ ,  $280 \times 280$  and  $400 \times 400$  cells have been used to discretize the computational domain  $[-2, 2] \times [-2, 2]$ . The diameter of the cylinder is  $D = 1$  and its center is located at  $(0,0)$ . The cylinder wall is assumed to be adiabatic. The boundary conditions for all test cases are for supersonic inflow at the boundary  $x = -2$ , and those for supersonic outflow for all other boundaries. Second order accuracy except for extrema is reached with the MUSCL scheme.

Figure 9 shows the Mach number contours. We observe a sharply resolved bow shock. Some of the flow in the wake of the cylinder exits the domain at a Mach number lower than one, and supersonic outflow boundary conditions are not correct in this region. However, the area is small and does not seem to affect the solution.

The skin friction profiles obtained from the New Simplified method with and without weighted

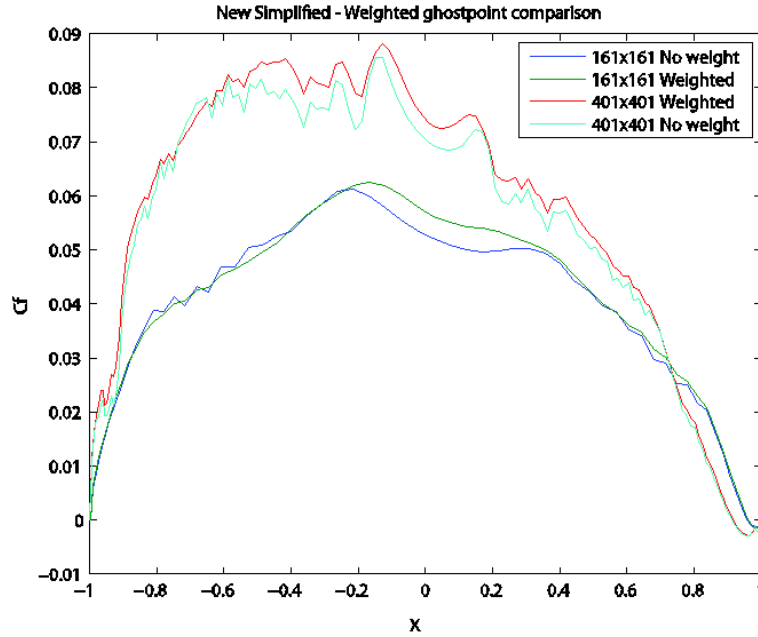


Figure 10: Comparison of the skin friction coefficient obtained from the weighted ghost point New Simplified Method and the New Simplified method without weighted ghost points for laminar flow over an adiabatic circular cylinder at  $M_\infty = 3$  and  $Re_D = 500$ .

ghost points are shown in figure 10. From these results we see that some of the bumps become smaller or disappear completely, as was the idea of improving the accuracy by weighting the ghost points. Without the weights the embedded boundary is assumed to lie in the middle between ghost and fluid points, which is usually not the case, and we believed this to be a reason for the bumps. With the weights one attempts to have the ghost point velocity components better reflect the actual location of the embedded boundary.

The comparison of the skin friction coefficient obtained from the New Simplified method and the Simplified method is shown in figure 11. In this plot it is evident that the New Simplified method is closer to the reference body-fitted skin friction profile from [10]. Thus, we can say that the New Simplified method performs better than the Simplified method for viscous flow as well.

In figure 12 the skin friction is plotted for various grid sizes and compared to the body-fitted results from [10]. As the resolution increases the bumps in the skin friction coefficient become more evident. The results from the finest grid are closest to the reference solution in the very front and rear parts of the cylinder, while the coarsest grid results actually looks like the best solution for  $-0.3m < x < 0.7m$ . Thus, no clear grid convergence is shown. Kupiainen and Sjögreen [10] achieve grid convergence of the skin friction for the current test case by four grid refinement patches. However, their results also suffer from bumps, which are much smaller than ours though due to their much finer grid.

The time stepping is stopped when the residual of the continuity equation reaches  $10^{-6}$ . The convergence history for the  $281 \times 281$  grid is shown in figure 13.

### *Supersonic Flow past a NACA0012 Airfoil with Compressible Navier-Stokes Equations*

In order to further verify the New Simplified method versus a well documented laminar supersonic flow, the flow past a NACA0012 airfoil has been considered. The following parameters

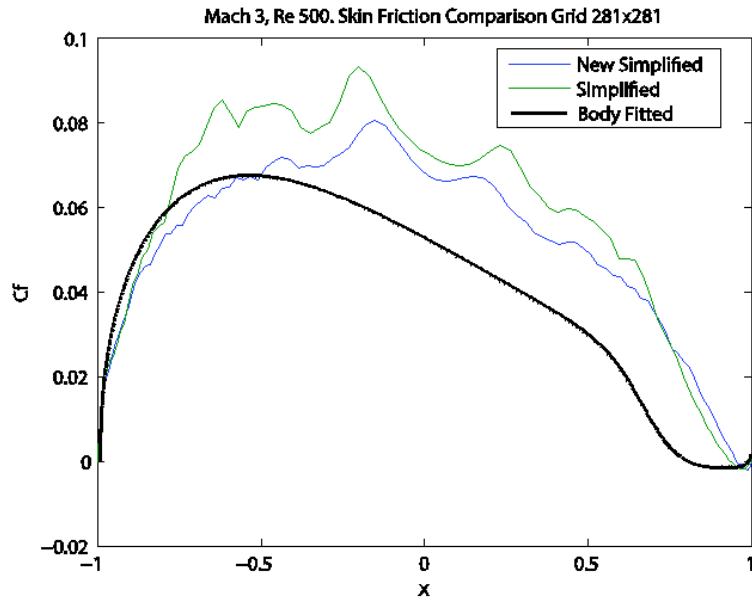


Figure 11: Comparison of the skin friction coefficient obtained from the New Simplified method and the Simplified method with a body-fitted solution from [10] for laminar flow over an adiabatic circular cylinder at  $M_\infty = 3$  and  $Re_D = 500$ .

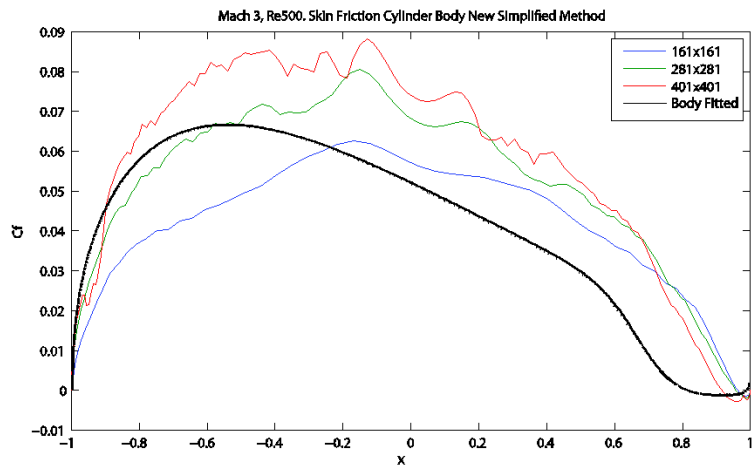


Figure 12: Skin friction profile obtained from the New Simplified method with grid refinement compared with a reference skin friction profile from a body-fitted solution in [10] for laminar flow over an adiabatic circular cylinder at  $M_\infty = 3$  and  $Re_D = 500$ .

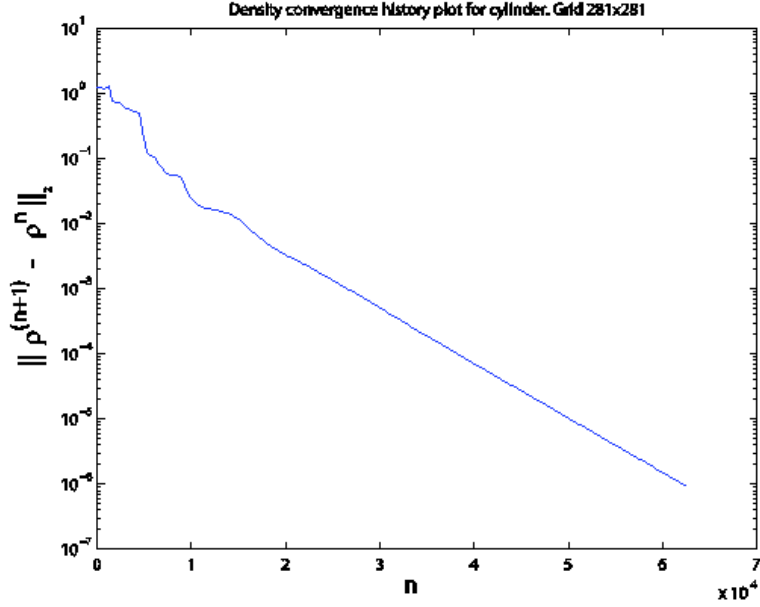


Figure 13: Convergence history with the New Simplified method for supersonic laminar flow over an adiabatic circular cylinder at  $M_\infty = 3$  and  $Re_D = 500$ .

have been used: Freestream Mach number  $M_\infty = 2$ , angle of attack  $\alpha = 10^\circ$ , and freestream Reynolds number  $Re_\infty = 1000$ . Three grids with  $400 \times 200$ ,  $600 \times 300$  and  $800 \times 400$  cells have been used to discretize the computational domain  $[-0.75, 2.25] \times [-0.75, 0.75]$ . The chord length of the airfoil is  $c = 1$ , whose leading edge is located at the origin. In this simulation the MUSCL scheme is applied to get second order accuracy, except for extrema. Supersonic inflow boundary conditions are used at the inflow  $x = -0.75$ , i.e. besides freestream density and pressure the inflow velocity components are set as  $u = M_\infty c_\infty \cos(\alpha)$  and  $v = M_\infty c_\infty \sin(\alpha)$ , where  $c_\infty$  is the freestream speed of sound. Supersonic outflow conditions are used at all other boundaries.

The residual measure  $\|\rho^{n+1} - \rho^n\|_2$  is reduced from about 1 to  $10^{-6}$  in about 63000 time steps, as the convergence history for the finest grid shows in figure 13.

The choice of the fluid points to mirror the ghost points near the leading edge is illustrated in figure 15. The choice of the fluid points depends on the angle of the normal component with respect to the negative x-axis as shown in figure 2 and equation (16).

The Mach number contours computed with the New Simplified method are plotted in figure 16. To compare the present results qualitatively, the work of De Palma et al. [5] using a Cartesian grid method has been used. Figure 17 shows the Mach number contours extracted from De Palma et al.'s plot 13 for a larger domain. From the qualitative comparison of figure 16 with the current results and figure 17 from [5], we see that we have good agreement. The shock waves and the wake exit the domain at the same locations in both simulations. Since the grid used with the New Simplified method is equidistant the bow shock wave is more refined at the outer regions. Shock wave reflections are visible where the bow shock exits the domain, but they are small. Because De Palma et al. [5] used a Cartesian grid with local grid refinement, their resolution around the airfoil is good, while they have less points in the outer regions.

The pressure coefficient along the airfoil surface is plotted in left of figure 18. The New Simplified method suffers from wavelike bumps. Although they get smaller with grid refinement,

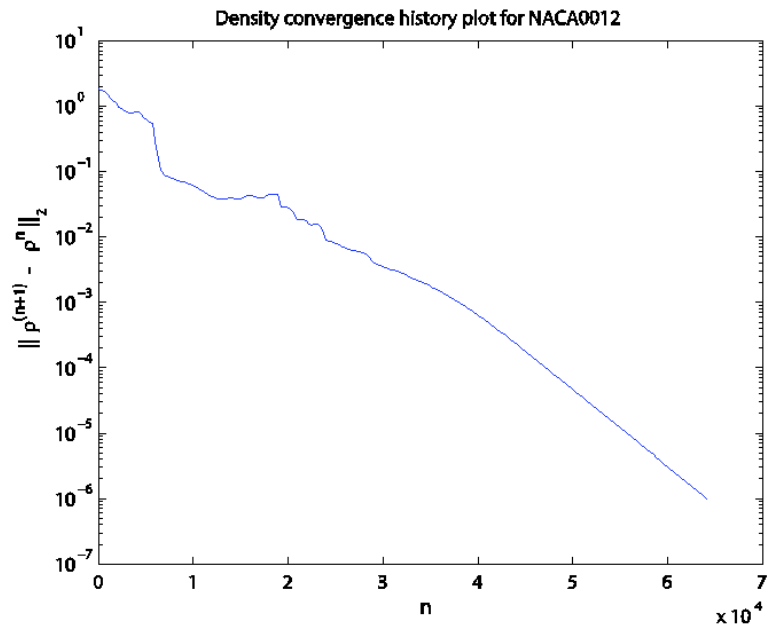


Figure 14: Convergence history for supersonic flow past a NACA0012 airfoil at a  $M_\infty = 2$ ,  $\alpha = 10^\circ$  and  $Re_\infty = 1000$  on a  $801 \times 401$  grid.

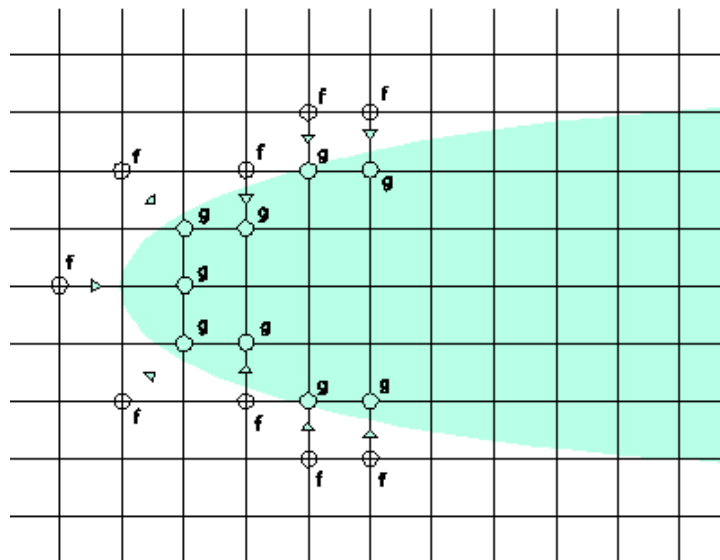


Figure 15: Choice of fluid points for ghost points near the leading edge of a NACA0012 airfoil.

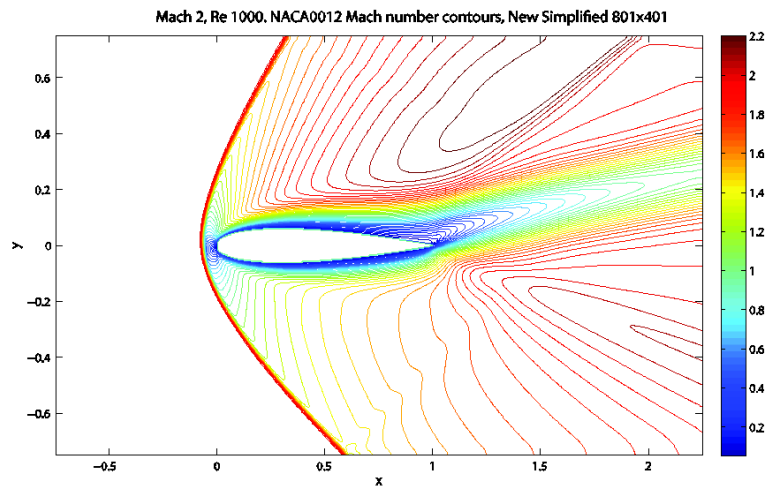


Figure 16: *Mach number contours for a NACA0012 airfoil obtained from the New Simplified method at a  $M_\infty = 2$ ,  $\alpha = 10^\circ$  and  $Re_\infty = 1000$  on a  $801 \times 401$  grid .*

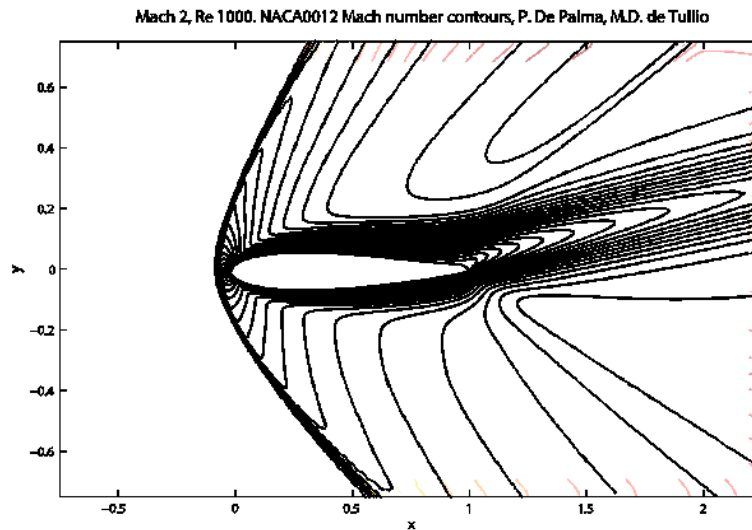


Figure 17: *Mach number contour results from De Palma et al. [5] in the domain  $[-0.75, 2.25] \times [-0.75, 0.75]$  at  $M_\infty = 2$ ,  $\alpha = 10^\circ$  and  $Re_\infty = 1000$  on  $500 \times 500$  grid with local grid refinement.*

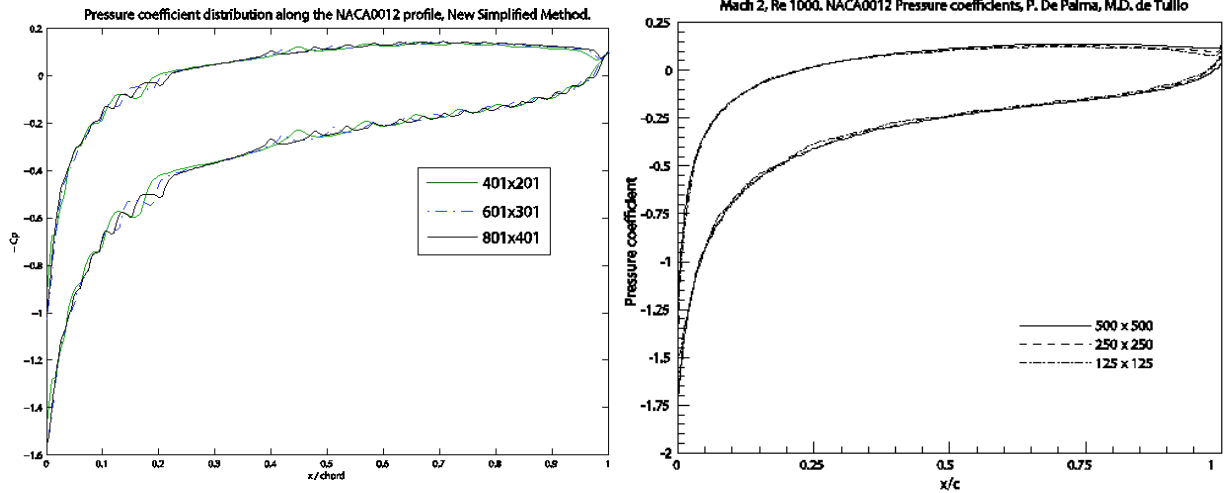


Figure 18: Pressure coefficient for a NACA0012 airfoil at  $M_\infty = 2$ ,  $\alpha = 10^\circ$  and  $Re_\infty = 1000$  on a  $801 \times 401$  grid. Left: New simplified method. Right: De Palma et al. [5].

**Table 1:** Drag and lift coefficients for supersonic flow around a NACA0012 airfoil at  $M_\infty = 2$ ,  $\alpha = 10^\circ$  and  $Re_\infty = 1000$ .

Reference	Mesh	$C_D$	$C_L$
Müller [13]	49x17 (C-grid)	0.2379	0.3253
	97x33 (C-grid)	0.2484	0.3388
	193x65 (C-grid)	0.2515	0.3388
De Palma et al. [5]	125x125 (Cartesian with local grid refinement)	0.2448	0.3296
	250x250 (Cartesian with local grid refinement)	0.2485	0.3335
	500x500 (Cartesian with local grid refinement)	0.2514	0.3353
New Simplified method	401x201 (Equidistant Cartesian grid)	0.2354	0.3335
	601x301 (Equidistant Cartesian grid)	0.2525	0.3400
	801x401 (Equidistant Cartesian grid)	0.2597	0.3421
Cambier, in [3]	193x72	0.2535	0.3427

they are still visible. Other than that, the shape and values of the pressure coefficient are fairly similar to the results of De Palma et al. [5] in the right of figure 18.

The lift and drag coefficients calculated are compared to the results of [5, 13, 3] in table 1. Note that the viscosity is taken as a constant and the airfoil wall has stagnation temperature in the results from the GAMM-workshop [3] considered by [5, 13], while the present results use the Sutherland law for viscosity and assume the airfoil wall to be adiabatic. The calculated drag and lift coefficients obtained with the New Simplified method are close to the other results in table 1. Thus, the wavelike bumps observed in the left of figure 18 even out each other out in total. However, the drag coefficient computed with the New Simplified method seems to need more points to get grid convergence.

### Supersonic Flow around a 2D F-22 Fighter Aircraft

To show the flexibility of the new simplified ghost point treatment, supersonic flow around an even more complex geometry has been considered, namely a 2D model of the F-22 fighter aircraft. The profile has been found on the websites of the United States Air Force (USAF)

[17]. The F-22 was chosen because of its similarity to the F-35 JSF aircraft that Norway has ordered. The jet engines have their own boundary conditions to simulate flow from the engines. There is little scientific value in this simulation, other than to show that there are few limits to the geometry of the embedded boundary with the use of the New Simplified or the Simplified method. A grid with 500x400 cells has been used to discretize the computational domain . The aircraft is 18.9 meters long [17]. To get a big jet from the engines the inviscid case with the compressible Euler equations has been used with a free stream Mach number  $M_\infty = 2$ . The outflow at the engine outlets has been set to a Mach number of 3, i.e.  $M_{jet} = 3$ , a density of  $\rho_{jet} = \rho_\infty$  and a pressure of  $p_{jet} = p_\infty$ . The ghost point values near the engine outlets were set equal to the engine outlet conditions. First order accuracy is reached with the first order local Lax-Friedrichs method.

The Mach number contours in Fig. 19 show the bow shock close to the blunt leading edge of the aircraft and expansions over the wing tips. The jet exiting the two jet engines expands and forms a barrel shock.

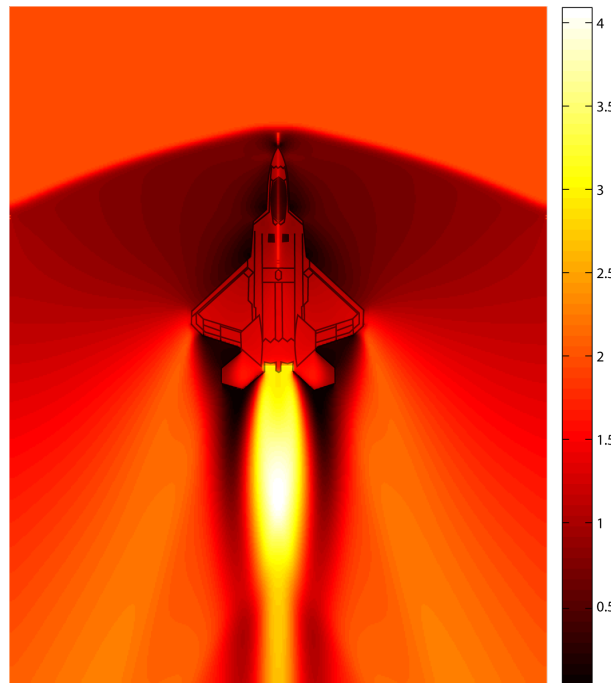


Figure 19: *Mach number contours of supersonic flow at  $M_\infty = 2$  over a 2D model of the F-22 fighter aircraft with engine outlet Mach number  $M_{jet} = 3$ .*

## Conclusions

We have presented a Cartesian grid method using simplified ghost point treatments at embedded boundaries for computing inviscid and viscous compressible flows around complex geometries. The method can give first or second order accuracy and is easy to implement for two-dimensional problems. The method has been verified versus well documented steady test problems in supersonic flow regimes using inviscid flow and viscous flow at moderate Reynolds numbers. We find that more grid points must be used to achieve high resolution near the body and in regions of high flow gradients in comparison with methods that use local grid refinement or have gridless points near boundaries. Several numerical tests have been performed to demonstrate the accuracy, robustness and versatility of the proposed method. The numerical results

obtained indicate that the use of the New Simplified method leads to an improvement over the Simplified method. The results from the New Simplified method are comparable, but not as accurate as other more complex methods.

For future work it would be interesting to further develop the method to compute three-dimensional problems. The order of accuracy could be increased, and it is natural to look at the implementation of local grid refinement. If we get higher resolution in areas of interest, we could solve for smaller scales and could increase the Reynolds number. A more pressing matter is to further develop and test the calculation of the skin friction coefficient, as it has proven to be very sensitive to any change in the methods used to calculate it. Lastly, the weighted ghost point method has potential for improvement.

### Acknowledgements

The contributions by M. Asif Farooq are gratefully acknowledged.

### References

- [1] Ames Research Staff Equations, tables and charts for compressible flow NACA Report 1135, 1953.
- [2] M.Berger and J.Aftosmis Progress towards a Cartesian cut-cell method for viscous compressible flow AIAA Paper 2012-1301, 2012.
- [3] M.Bristeau, R.Glowinski, J.Periaux and H.Viviani *Numerical Simulation of Compressible Navier-Stokes Flows* Vieweg, Braunschweig, 1987.
- [4] A.Dadone and B.Grossman Ghost-cell method for analysis of inviscid three-dimensional flows on Cartesian-grids *Computers & Fluids*, **vol.36**, 1513–1528, 2007.
- [5] P.De Palma, M. D.de Tullio, G.Pascasio and M.Napolitano An immersed-boundary method for compressible viscous flows *Computers & Fluids*, **vol.35**, 693–702, 2006.
- [6] M.Farooq *Cartesian Grid Method for Compressible Flow Simulation* PhD thesis, NTNU, 2012.
- [7] M.Farooq and B.Müller Accuracy of the Cartesian grid method for hyperbolic conservation laws using standard and simplified ghost point treatments at the immersed boundary *Journal of Structural Mechanics*, **vol.44**(3), 279–291, 2011.
- [8] M.Farooq and B.Müller Cartesian grid method for compressible flows to compute shock waves *Proceedings of International Bhurban Conference on Applied Sciences and Technology*, Islamabad, Pakistan, January 9-12, 2012.
- [9] L. S.Kim, K.Nakahashi, H. K.Jeong and M. Y.Ha High density mesh flow computations by building cube method *Journal of Mechanical Science and Technology*, **vol.21**, 1306–1319, 2007.
- [10] M.Kupiainen and B.Sjögreen A Cartesian embedded boundary method for the compressible Navier-Stokes equations *Journal of Scientific Computing*, **vol.41**, 94–117, 2009.
- [11] R.Mittal and G.Iaccarino Immersed boundary methods *Annual Review of Fluid Mechanics*, **vol.37**(1), 239–261, 2005.
- [12] B.Müller Linear stability condition for explicit Runge-Kutta methods to solve the compressible Navier-Stokes equations *Mathematical Methods in the Applied Sciences*, **vol.12**, 139–151, 1990.
- [13] B.Müller Navier-Stokes solution for laminar transonic flow over a NACA0012 airfoil FFA Report 140, FFA, The Aeronautical Research Institute of Sweden, Stockholm, 1986.

- [14] L.Schneiders, D.Hartmann, M.Meinke and W.Schröder An accurate moving boundary formulation in cut-cell methods *Journal of Computational Physics*, **vol.235**, 786–809, 2013.
- [15] B.Sjögreen and N.Petersson A Cartesian embedded boundary method for hyperbolic conservation laws *Communications in Computational Physics*, **vol.2(6)**, 1199 – 1219, 2007.
- [16] A.Skøien Cartesian grid method for the compressible Navier-Stokes equations Master's Thesis, NTNU, 2012.
- [17] United States Air Force Website <http://www.af.mil/shared/media/ggallery/hires/AFG-060411-002.jpg>.